

LA-UR-21-24959

Accepted Manuscript

Thermal and solubility effects on fault leakage during geologic carbon storage

Meguerdijian, Saro
Pawar, Rajesh J.
Harp, Dylan Robert
Jha, Birendra

Provided by the author(s) and the Los Alamos National Laboratory (2022-04-25).

To be published in: International Journal of Greenhouse Gas Control

DOI to publisher's version: 10.1016/j.ijggc.2022.103633

Permalink to record:

<http://permalink.lanl.gov/object/view?what=info:lanl-repo/lareport/LA-UR-21-24959>



Los Alamos National Laboratory, an affirmative action/equal opportunity employer, is operated by Triad National Security, LLC for the National Nuclear Security Administration of U.S. Department of Energy under contract 89233218CNA000001. By approving this article, the publisher recognizes that the U.S. Government retains nonexclusive, royalty-free license to publish or reproduce the published form of this contribution, or to allow others to do so, for U.S. Government purposes. Los Alamos National Laboratory requests that the publisher identify this article as work performed under the auspices of the U.S. Department of Energy. Los Alamos National Laboratory strongly supports academic freedom and a researcher's right to publish; as an institution, however, the Laboratory does not endorse the viewpoint of a publication or guarantee its technical correctness.

1 Thermal and Solubility Effects on Fault Leakage during
2 Geologic Carbon Storage

3 Saro Meguerdijian^{a,b}, Rajesh J. Pawar^b, Dylan R. Harp^{b,c}, Birendra Jha^{a,*}

4 ^a*Department of Chemical Engineering and Materials Science, University of Southern*
5 *California, Los Angeles, CA 90089, United States*

6 ^b*Earth and Environmental Sciences Division, Los Alamos National Laboratory, Los*
7 *Alamos, NM 87544, United States*

8 ^c*The Freshwater Trust, Portland, OR 97205, United States*

9 **Abstract**

Geologic carbon storage (GCS) is a promising method for reducing anthropogenic CO₂ emissions to the atmosphere. To safely deploy GCS in the field, it is necessary to assess risks and the effect of uncertainty on safe storage. The effect of uncertainty can be quantified using batches of simulations, but the high computational costs of high-resolution simulations necessitate use of reduced-order models (ROMs). Previous work involves ROMs for quantifying the risk of different potential leakage paths from storage reservoirs to shallow formations. However, previous studies on development of fault-leakage ROMs have limited numbers of uncertain parameters and do not explicitly examine impacts of CO₂ solubility and thermal stresses on fault reactivation, which can generate high permeability pathways and compromise CO₂ storage. In this study, we analyze an ensemble of simulations considering CO₂ leakage from a storage reservoir to a shallow aquifer through a fault while varying a number of uncertain parameters related to thermo-hydro-mechanical properties and CO₂ injection. We show the effects of solubility on: free-phase CO₂-leakage rates, brine-leakage rates, and poroelastic fault destabilization. We find that CO₂ solubility is more important for estimating free-phase CO₂-leakage rates compared to brine-leakage rates or poroelastic fault destabilization. We also find that thermal stresses and overpressures have different spatial distributions within the fault, indicating that the spatial variability of overpressures due to variation in flow parameters does not

*Corresponding author

Email address: bjha@usc.edu (Birendra Jha)

necessarily make the spatial variability of thermal stresses negligible. We suggest the use of the CO₂ phase-change path as a variable in future fault-leakage ROMs.

10 *Keywords:* Geologic carbon storage, reduced-order model, fault leakage, CO₂,
11 fault reactivation

12 **1. Introduction**

13 Geologic carbon storage (GCS) is considered a promising method for reduc-
14 ing CO₂ emissions to the atmosphere (IPCC, 2005). With the enactment of the
15 recent §45Q statute (26 USC §45Q, 2019), many billions of dollars of tax credits
16 are set to incentivize the growth of carbon capture and storage significantly over
17 the next decades. However, concerns exist over the safety of CO₂ storage sites
18 (White & Foxall, 2016; Newell & Ilgen, 2019). Risk assessment is essential to
19 both the technical and economic viability of GCS projects. Probabilistic en-
20 sembles of simulations are a prominent way to quantify risk under uncertainty
21 because of their ability to integrate the various complexities of the subsurface;
22 however, they can often be too computationally expensive or numerically chal-
23 lenging to execute. Reduced-order models (ROM) are one way to overcome this
24 problem and so are favored for applications such as site-screening (Middleton
25 et al., 2020). ROMs reduce the computational burden of simulations by captur-
26 ing only the physics essential to a given risk assessment problem. ROMs have
27 been applied to field cases (Onishi et al., 2019).

28 Comprehensive risk assessment includes identification of uncertain variables
29 and impact of uncertainty on risks. It involves the risk of fault reactivation
30 and subsequent change in fault permeability, although these effects are not
31 straightforward to capture (Rinaldi et al., 2014; Zheng et al., 2021). A fault
32 may reactivate and cause substantial changes in permeability (Guglielmi et al.,
33 2017; Tran & Jha, 2021), resulting in a high permeability pathway to the sur-
34 face, potentially causing loss of containment of stored CO₂ and associated ge-
35 omechanical deformation patterns across the fault (Meguerdijian & Jha, 2021).

36 CO₂ is partially miscible in brine. The dissolution process depends on CO₂
37 pressure and temperature, both of which can change with time as CO₂ migrates
38 within the reservoir and potentially through a fault. It is believed that moni-
39 toring dissolved CO₂ in brine can assist with monitoring CO₂ plume migration,
40 solubility trapping, and groundwater contamination risk associated with CO₂
41 storage (Keating et al., 2010). However, a limitation of the high computational
42 cost of storage simulations is that, for the purposes of producing ROMs, the
43 sample size of simulations to adequately cover the parameter space of even a
44 few uncertain variables can be quite large. When combined with coupled flow
45 and geomechanics, the computational burden can become substantial, such that
46 even training ROMs for use in uncertainty quantification becomes challenging.

47 In previous research, ROMs have been generated for simulations of wellbore
48 leakage (Harp et al., 2016), aquifer impacts (Keating et al., 2016; Bianchi et al.,
49 2016), fault leakage without geomechanics (Lu et al., 2012), and preliminary
50 work on fault leakage as either a plane (Lindner, 2020) or a continuum with
51 aseismic slip (White et al., 2017). These fault-leakage ROM studies include
52 those involving a limited number of uncertain variables (around five, though
53 possibly after a sensitivity analysis of potential inputs) or simplified physics,
54 such as the assumption of parallel plate flow. While these studies provide im-
55 portant information regarding the effects of fault slip or initial steps toward
56 development of a fault-leakage ROM that can be incorporated into risk assess-
57 ment frameworks, such as NRAP-IAM-CS (Pawar et al., 2016), they do not
58 explore the effects of solubility or thermal stresses in detail.

59 In this paper, we identify insights for future ROM development by investi-
60 gating the physical process of fault leakage. We present an analysis of brine and
61 CO₂ leakage rates through faults and their association with fault destabilization
62 induced by CO₂ injection, with particular focus on CO₂ solubility and thermal
63 stresses. We use a 3D model to simulate leakage from a storage reservoir through
64 a fault to a shallow aquifer, and we consider 19 uncertain variables associated
65 with fluid flow through faults. We compute poroelastic destabilization, temper-
66 ature changes, and thermal stress changes within the fault across an ensemble

67 of realizations. We consider the effects of solubility on fault stability. We show
68 that in spite of substantial variations in input parameters, thermal stresses can
69 still exert significant effects on fault destabilization and thereby on changes in
70 fault permeability and resulting leakage rates. For the parameter space used
71 in this study, we note that the spatial distribution of thermal stresses in the
72 fault is different from that of overpressures. The two effects occur in different
73 portions in the fault in such a manner that the spatial variability of one does not
74 render the spatial variability of the other negligible. Moreover, we show that
75 CO₂ dissolution affects free-phase CO₂ leakage rates, where “free-phase” refers
76 to liquid, vapor, and supercritical phases combined but not CO₂ dissolved in
77 brine. The effect of solubility on brine leakage rates and poroelastic fault desta-
78 bilization is minimal. We draw conclusions as to how to generate fault-leakage
79 ROMs which incorporate these findings.

80 **2. Methods**

81 *2.1. Description of the physics and constitutive equations*

82 We used the Finite Element Heat and Mass Transfer (FEHM) code to
83 perform fully-coupled 3D multiphase simulations with heat and mass trans-
84 fer (Zyvoloski et al., 2015). The relevant equations have been described previ-
85 ously (Zyvoloski et al., 1999). We used the Pylith-FlowSim simulator (Jha &
86 Juanes, 2014; Zhao & Jha, 2019, 2021; Tiwari et al., 2021) to conduct geome-
87 chanical analyses using the outputs of FEHM and one-way flow-to-mechanics
88 coupling. Given that this study is concerned with the risks to fault stability
89 due to injection in a deep aquifer and leakage from a deep aquifer to a shallow
90 aquifer, it is safer to assume that the mechanics-to-flow coupling is negligible, as
91 the presence of mechanics-to-flow coupling would tend to produce lower pressure
92 estimates and consequently lower leakage and risk of fault reactivation.

93 Mechanics-to-thermal coupling is considered insignificant because heat flow
94 occurs by two main mechanisms in the reservoir: (1) conduction and (2) con-
95 vection. Regarding conduction, the thermal conductivity of a cell depends on

96 the relative fractions of brine, rock, and supercritical CO₂ (scCO₂). Mechanics
 97 would change this by changing the porosity. However, the porosity changes are
 98 expected to be small, as the change in porosity due to pressure is proportional
 99 to the inverse of the drained bulk modulus (Biot & Willis, 1957; Coussy, 2004,
 100 Eqns. 4.21c, 4.35, 4.44; as given by White et al., 2019, Eqn. 4). The drained
 101 bulk modulus of a reservoir can be on the order of GPa, leading to small porosity
 102 changes in the response to pressure changes on the order of MPa. Thermal con-
 103 traction would also be small, considering that the volumetric thermal expansion
 104 coefficient of many common minerals is on the order of 10⁻⁵/°C (Robertson,
 105 1988, Table 9). This would limit the amount of convection which would occur
 106 as a result of thermomechanical deformation. Consequently, in this study, one-
 107 way coupling is safer for the estimation of fault reactivation risk than two-way
 108 coupling.

109 The numerical formulation of (Jha & Juanes, 2014) is used to calculate
 110 poroelastic effects while thermal stresses in the fault are calculated separately.
 111 The change in the Coulomb Failure Function (CFF) (also known as the Coulomb
 112 failure stress) (Reasenberg & Simpson, 1992; Scholz, 2019) is used to estimate
 113 fault destabilization due to poroelastic effects:

$$\Delta\text{CFF} = \Delta|\tau| + \mu_f \Delta\sigma'_n \quad (1)$$

114 where τ is the shear stress on the fault, μ_f is the fault's static coefficient of
 115 friction, and σ'_n is the effective normal stress (assumed positive in tension) on the
 116 fault. We consider only changes in the CFF in our work to avoid specifying an
 117 initial stress state, which can have substantial uncertainties due to its methods of
 118 measurement (Burghardt & Appriou, 2021) and is unnecessary for establishing
 119 this study's conclusions concerning fault destabilization. The thermal stresses
 120 are volumetric in nature and are calculated as (Coussy, 2004, Eqn. 4.24):

$$\boldsymbol{\sigma}_T = -3\alpha_s K_{dr}(T - T_0)\mathbf{1} \quad (2)$$

121 where $\mathbf{1}$ is the rank-2 identity tensor, K_{dr} is the drained bulk modulus, T is the
 122 current temperature, T_0 is the initial temperature, and α_s is the linear thermal

123 expansion coefficient of the solid phase. Note that cooling of a fault can lead to
124 destabilization depending on the reservoir conditions (Jacquey et al., 2015).

125 *2.2. The model*

126 Our conceptual model is shown in Figure 1. The model consists of a deep
127 aquifer, a caprock, a shallow aquifer, overburden, and a two-part fault. The
128 fault consists of a fault core and damage zone and follows the description given
129 by (Johri, 2012). The fixed parameters of the reservoir model are listed in Ta-
130 ble 1. The varying parameters of the reservoir model are shown in Table 2
131 along with their respective ranges. The values of the varying parameters are
132 sampled uniformly (uniformly in the logarithmic domain for permeabilities) or
133 with equal probability for the discrete values using Latin Hypercube Sampling
134 (LHS) (Helton & Davis, 2002). Note that a reduced-order model is not gen-
135 erated in this study, but rather an ensemble of realizations across the range
136 of these varying parameters is analyzed. The FEHM flow simulation model is
137 constructed using a mesh (termed the “FEHM mesh”) that has evenly spaced
138 cells in all directions, except for a geometrically spaced region in the x-direction
139 near $x=0$ m to resolve the fault. The cell centroids of this mesh are then used
140 to make another mesh (termed the “Pylith mesh”). The Pylith mesh is used
141 with Pylith-FlowSim, and pressure values from the FEHM mesh are assigned to
142 the centroids of the Pylith mesh. This allows us to couple FEHM to Pylith to
143 perform geomechanical simulations using pressures directly from FEHM. Con-
144 structing the Pylith mesh in this manner avoids any loss in accuracy due to
145 interpolation of pressure, which will be required in case of two arbitrary meshes
146 for flow and geomechanics.

147 The reservoir is initialized to a steady-state geothermal and hydrostatic gra-
148 dient. The boundary conditions for fluid flow and heat transfer are no-flow on all
149 boundaries, except for the shallow aquifer, which has constant pressure outflow-
150 only boundaries for both brine and CO_2 . This increases the pressure gradient
151 from the injection well to the shallow aquifer and so promotes leakage, enabling
152 a conservative leakage estimate. Note that pressure does increase within the

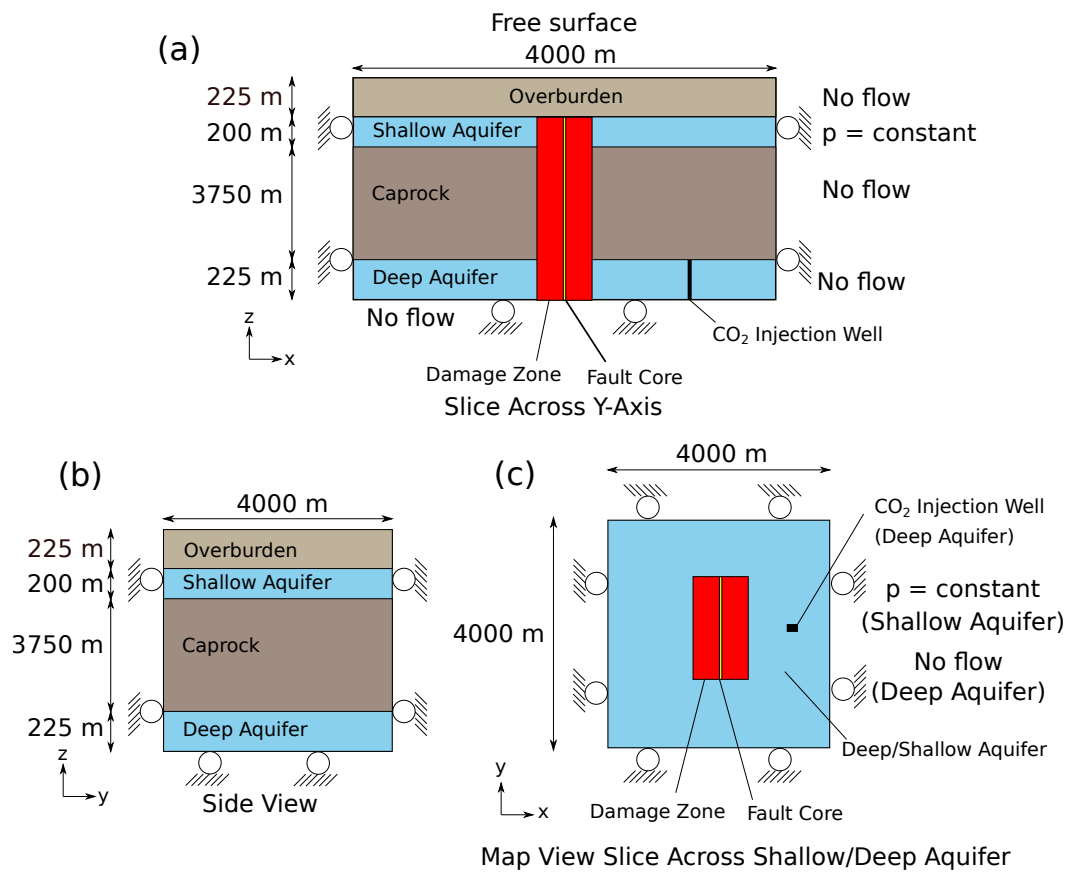


Figure 1: A schematic of the fault-leakage model problem.

Parameters	Value
Deep aquifer thickness (m)	225
Caprock thickness (m)	3750
Shallow aquifer thickness (m)	200
Overburden thickness (m)	225
Density of the rock (solid phase) (kg/m ³)	2650
Specific heat capacity of the rock (solid phase) (J/(kg·K))	920
Surface temperature (at the top of the domain)(°C)	10
Geothermal gradient (°C/km)	8.4
Temperature at the bottom of the domain (°C)	47
Pressure at the top of the domain (MPa)	0.1
Porosity of the caprock (dimensionless)	0.1
Porosity of the overburden (dimensionless)	0.1
Permeability of the caprock (m ²)	10 ⁻¹⁸
Permeability of the overburden (m ²)	10 ⁻¹⁸
CO ₂ injection temperature (°C)	32
Biot coefficient of the domain (dimensionless)	0.8
Biot coefficient of the fault (b , dimensionless)	0.8
Coefficient of static friction for the fault (μ_f , dimensionless)	0.6
Height of the domain (m)	4400
X-width of the domain (m)	4000
Y-width of the domain (m)	4000
Well top z-coordinate (m)	225
Well bottom z-coordinate (m)	0
Total injection time (years)	10
Total simulation time (years)	30
Relative permeability model	linear
Fault x-coordinate (m)	0
Fault y-coordinates (m)	[-1700, 1700]
Fault z-coordinates (m)	[75, 4175]

Table 1: Fixed parameters of the reservoir model.

Parameters	Range/Set
Fault core permeability ($\log_{10}(\text{m}^2)$)	[-18,-12]
Fault core porosity (dimensionless)	[0.001,0.1]
Damage zone permeability ($\log_{10}(\text{m}^2)$)	[-15,-12]
Damage zone porosity (dimensionless)	[0.001,0.1]
Shallow aquifer permeability ($\log_{10}(\text{m}^2)$)	[-14,-12]
Shallow aquifer porosity (dimensionless)	[0.05,0.5]
Deep aquifer permeability ($\log_{10}(\text{m}^2)$)	[-14,-12]
Deep aquifer porosity (dimensionless)	[0.05, 0.35]
Fault core thickness (m)	[0.0, 0.5]
Damage/fault zone thickness (includes fault core thickness) (m)	{33.33,70.85}
Fault permeable length (m)	{800,1600,2400}
Rock conductivity (W/(m·K))	[1.0, 6.0]
Well x-coordinate (m)*	{154.26,248.10,388.86}
Well y-coordinate (m)	{-200,0,200}
Well rate (kg/s)	[7.5, 25]
Solubility of CO ₂	{soluble, insoluble}
Volumetric thermal expansion coefficient ($^{\circ}\text{C}^{-1}$)	[10^{-5} , 5×10^{-5}]
Poisson's ratio (dimensionless)	[0.2,0.35]
Young's modulus (GPa)	[5,20]

Table 2: Varying parameters of the reservoir model. Square brackets denote a continuous, uniform distribution while brackets denote a discrete distribution. *The x-axis is at the center of the fault.

153 deep aquifer during injection under these boundary conditions. Injection occurs
154 through the well at depths of 4175-4400 m. The CO₂ injection rate is constant
155 during the injection period and zero after the injection period ends. The depths
156 are chosen such that the CO₂ passes from a supercritical state to a gas state
157 as it migrates from the deep aquifer to shallow aquifer through the fault. The
158 flow and transport solvers are coupled. Density changes with pressure, temper-
159 ature, and dissolved CO₂ concentration. CO₂ solubility changes as a function of
160 pressure, temperature, and salinity. As capillary pressure would tend to inhibit
161 CO₂ leakage, we neglect capillary pressures to obtain conservative estimates of
162 leakage and more easily draw conclusions from our simplified model.

163 The fault consists of a vertical fault core and damage zone whose properties
164 are considered equivalent properties (e.g. an upscaled permeability) and whose
165 parameter variations are meant to reflect the variety of conditions which can
166 occur in the subsurface. Faults can exhibit complex, time-dependent behavior
167 with slip, such as slip-dependent permeability followed by leakage and fracture
168 self-healing (Chester et al., 1993), and numerous mechanisms can be involved
169 in a fault’s history (Sibson, 1977). Fault core composition varies with distance
170 from the slip surface (Scholz, 2019), with asymmetry potentially across the fault
171 (e.g. pulverization on one side of the fault when rock stiffness values differ on
172 each side of the fault (Mitchell et al., 2011; Dor et al., 2006)). Fault zone
173 conceptual models include differences in the architecture of the fault (e.g. a
174 single fracture vs. a deformation zone, fractured rock around the core vs. solid
175 rock around the core) (Caine & Forster, 1999). In this work, we opt for a fault
176 model which focuses on the leakage amounts and selected stresses, incorporating
177 the uncertainties in the fault architecture through a two-part fault model (fault
178 core and damage zone), the use of equivalent permeabilities and porosities for
179 the fault, and a range of fault property values to capture the fault’s properties’
180 uncertainties. This is a simplified model and is not applicable in all cases. We
181 choose to increase the parameter uncertainties instead of the model complexity
182 to obtain clear causative relationships.

183 The permeabilities and porosities of the fault core and damage zone are

184 obtained by LHS. These values are then upscaled, with the resulting upscaled
185 permeabilities and porosities assigned to the mesh vertices in the x-direction
186 nearest to the fault. The fault is modeled as a zone consisting of a plane of cells
187 one-cell thick on each side of the fault’s center plane when the damage zone is
188 33.33 m thick and a region two-cells thick on each side of the fault when the
189 damage zone is 70.85 m thick. When the damage zone is 70.85 m thick, the
190 properties of the second sheet of cells furthest from the fault’s center plane are
191 those of the damage zone. In both cases, the first sheet of cells (those adjacent to
192 the fault’s center plane, here called the “inner fault zone cells”) have upscaled
193 properties incorporating both damage zone and fault core properties. These
194 upscaled properties are calculated using the following equations:

$$k_{fc,x}^* = \frac{x_{ib} - x_c}{\frac{L_{fc}}{k_{fc}} + \frac{x_{ib} - L_{fc}}{k_{dz}}} \quad (3)$$

$$k_{fc,y/z}^* = \frac{k_{fc}L_{fc} + k_{dz}(x_{ib} - L_{fc})}{x_{ib} - x_c} \quad (4)$$

$$\phi_{fc}^* = \frac{\phi_{fc}L_{fc} + \phi_{dz}(x_{ib} - L_{fc})}{x_{ib} - x_c} \quad (5)$$

197 where:

- 198 • $k_{fc,x}^*$ is the upscaled permeability in the x-direction of the inner fault zone
199 cells,
- 200 • $k_{fc,y/z}^*$ is the upscaled permeability in the y- and z-direction of the inner
201 fault zone cells,
- 202 • ϕ_{fc}^* is the upscaled porosity of the inner fault zone cells,
- 203 • x_{ib} is the thickness of the inner fault zone cells in the x-direction (equal
204 to 33.33 m),
- 205 • x_c is the x-coordinate of the center of the fault ($x_c = 0$ m in this case),
- 206 • L_{fc} is the fault core thickness,

- 207 • k_{fc} is the fault core permeability,
- 208 • k_{dz} is the damage zone permeability,
- 209 • ϕ_{fc} is the fault core porosity, and
- 210 • ϕ_{dz} is the damage zone porosity.

211 A low geothermal gradient is chosen (the value in Table 1 is roughly that of an
212 old continental craton (Lowell et al., 2014)); this allows for a more conservative
213 estimate of CO₂ solubility effects on Δ CFF and allows phase change to occur
214 within the fault. Phase change produces both temperature changes (which
215 induce thermal stresses) and substantial drops in density in the fault.

216 3. Results and analysis

217 3.1. Base Case

218 We performed a base case simulation to demonstrate the physics of the
219 model problem. Table 3 shows the parameters used in the base case. The case
220 does not take into account CO₂ solubility in brine, but the effect of solubility is
221 shown through comparison with results from the model with CO₂ solubility. The
222 damage zone permeability is about 7 mD while the deep aquifer permeability is
223 about 389 mD. The shallow aquifer permeability is about 405 mD. A corner of
224 the simulation domain is plotted in the following figures to show the properties
225 from the simulation in both the fault and aquifers. Figure 2 shows this cutout of
226 a corner of the domain with $x = 0$ m corresponding to the fault. The injection
227 rate is roughly 706,000 metric tons of CO₂ per year. Figure 3(a) shows that
228 water movement occurs around the well and within the fault both vertically up
229 the fault and laterally across the fault, with greater water movement occurring
230 in the fault areas closest to the well and vertically above. Such 3D patterns of
231 leakage have been missing in some of the earlier 2D modeling studies of leakage.
232 Water movement also occurs in the fault section within the shallow aquifer.
233 Figure 3(b) shows that water movement is substantially reduced both laterally

234 in the fault and within the shallow aquifer when solubility effects are included.
235 This indicates changes in the pattern of CO₂ spread, which we analyze further
236 below.

237 While the CO₂ plume travels a smaller distance laterally in the fault when
238 solubility effects are present, the fault is nevertheless pressurized across its per-
239 meable length. A substantial amount of CO₂ dissolution occurs within the fault.
240 Figure 4(a) and (b) show that the supercritical CO₂ (scCO₂) is present near
241 the injection well and within the fault, but the lateral spread of scCO₂ in the
242 fault is reduced when solubility is included. The same is observed with the
243 length of the plume across the top of the fault, in the shallow aquifer zone, in
244 Figure 4(c) and (d). Figure 4(e) shows that when solubility is present, dissolu-
245 tion of CO₂ limits the lateral spread of the free-phase CO₂ plume in the fault.
246 This is important because it shows how CO₂ may leak in both the free-phase
247 (undissolved) and the aqueous phase (dissolved), and why CO₂ monitoring ef-
248 forts should consider CO₂ solubility in cases where dissolved CO₂ may act as a
249 signature of CO₂ presence or risks such as elevated metal concentrations. The
250 pressure has a different distribution than the CO₂ saturation: Figure 5 shows
251 that, while initially pressurized according to the hydrostatic gradient in (a), the
252 fault is laterally pressurized nearly equally along the fault's permeable length
253 (y-direction), as shown in (b). This can be attributed to the relatively high
254 deep-aquifer permeability in comparison to the damage zone permeability.

255 The thermal stresses show a substantially different spatial distribution than
256 the poroelastic ΔCFF but with a similar magnitude, suggesting that thermal
257 effects are important for the evaluation of fault stability in this case. Figure 6(a)
258 and (b) show that the thermal gradient stays largely the same in the fault
259 except at the top, below the overburden. Figure 6(c) shows that the fault
260 itself warms slightly, but the top of the fault cools much more. This is due to
261 CO₂ vaporizing from a liquid phase to a gas phase, absorbing its latent heat of
262 vaporization from its surroundings and causing cooling (see Figure 7 for the phase
263 transition depths), and Joule-Thomson cooling from gaseous CO₂ expanding.
264 In terms of thermal stresses, Figure 6(d) shows that the thermal stresses within

265 the fault are slightly stabilizing (compressive), but those at the top of the fault
266 are significantly tensile and could potentially reactivate the fault depending on
267 the proximity of the initial stress state to the Mohr-Coulomb failure envelope.
268 In contrast, Figure 8(a) shows that the poroelastic ΔCFF is greatest slightly
269 above the bottom of the fault. This corresponds to the overpressure (shown
270 in Figure 8(b)) in the fault and above the deep aquifer. A difference appears
271 between the ΔCFF and pressure fields at the bottom of the fault, in the deep
272 aquifer region and immediately above it. As the pore pressures on both sides of
273 the fault are more equal in the deep aquifer than in the fault (where permeable
274 damage zone is surrounded by impermeable caprock), the reduction in effective
275 normal stress is greater in the region within the caprock than in the deep aquifer.
276 Therefore, while poroelastic effects promote destabilization deep in the domain
277 but above the deep aquifer in this case, thermal stresses promote destabilization
278 at shallow depths.

Parameters	Value
Fault core permeability ($\log_{10}(\text{m}^2)$)	-13.8114
Fault core porosity (dimensionless)	0.0134959
Damage zone permeability ($\log_{10}(\text{m}^2)$)	-14.1377
Damage zone porosity (dimensionless)	0.00549412
Shallow aquifer permeability ($\log_{10}(\text{m}^2)$)	-12.3988
Shallow aquifer porosity (dimensionless)	0.444103
Deep aquifer permeability ($\log_{10}(\text{m}^2)$)	-12.4161
Deep aquifer porosity (dimensionless)	0.315762
Fault core thickness (m)	0.483355
Damage/fault zone thickness (includes fault core thickness) (m)	33.333
Fault permeable length (m)	2400
Rock conductivity (W/m*K)	5.99166
Well x-coordinate (m)	154.265
Well y-coordinate (m)	0
Well rate (kg/s)	22.3783
Solubility of CO ₂	insoluble*
Volumetric thermal expansion coefficient ($^{\circ}\text{C}^{-1}$)	$2.15876 \cdot 10^{-5}$
Poisson's ratio (dimensionless)	0.20312
Young's modulus (GPa)	7.91083

Table 3: The varying parameters for the base case. *The base case results are for the insoluble case unless otherwise noted.

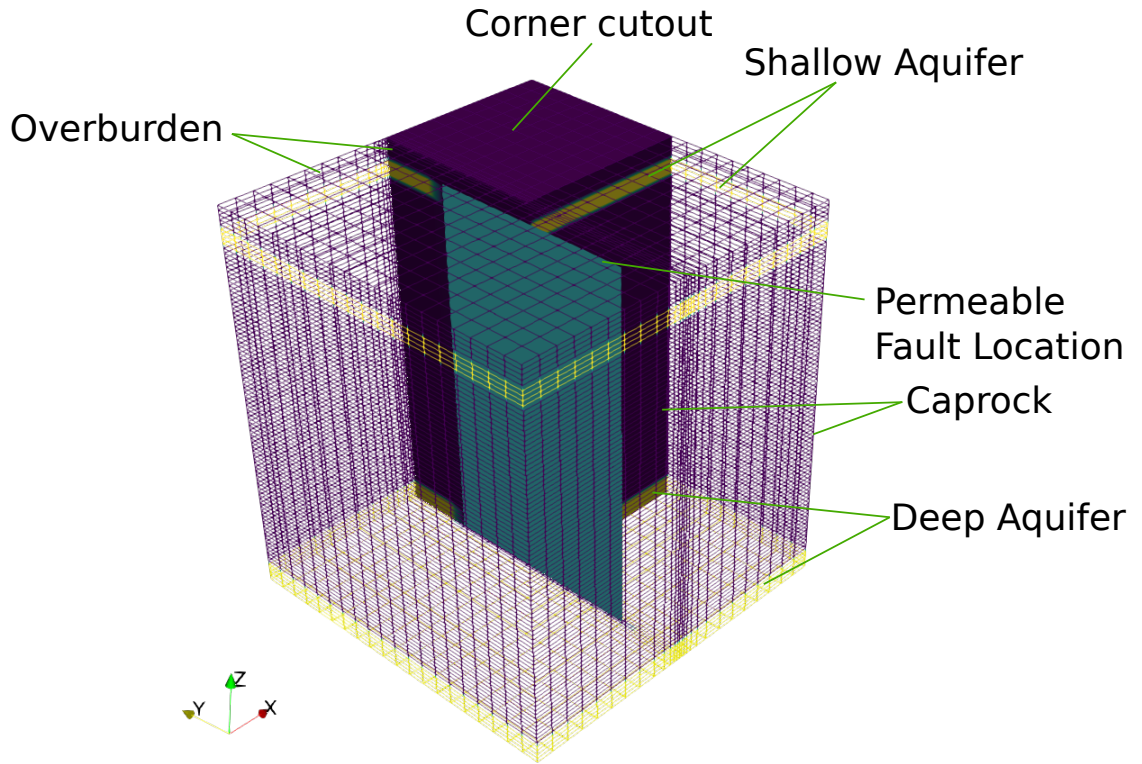


Figure 2: The location of the corner cutout and permeable portion of the fault in the base case figures. The corner cutout and permeable fault location are shown in solid colors. The entire simulation domain is shown using a wireframe drawing.

279 *3.2. Autocorrelation of inputs*

280 We sampled the uncertain parameters using LHS. A portion of numerical
 281 simulations did not complete due to numerical instabilities. We used 217 simu-
 282 lations and verified that the sampling is unbiased to a first-order approximation.
 283 Cumulative distribution functions of the inputs for the completed runs are shown
 284 in Figure S.1 in the supplementary information. Figure S.1 shows that the input
 285 distributions are sufficiently uniform.

286 It is apparent that the inputs do not have any substantial linear correla-
 287 tions between themselves. Figures S.2 and S.3 show that all the correlations
 288 have correlation coefficient values less than 0.3. Because of this, first-order lin-

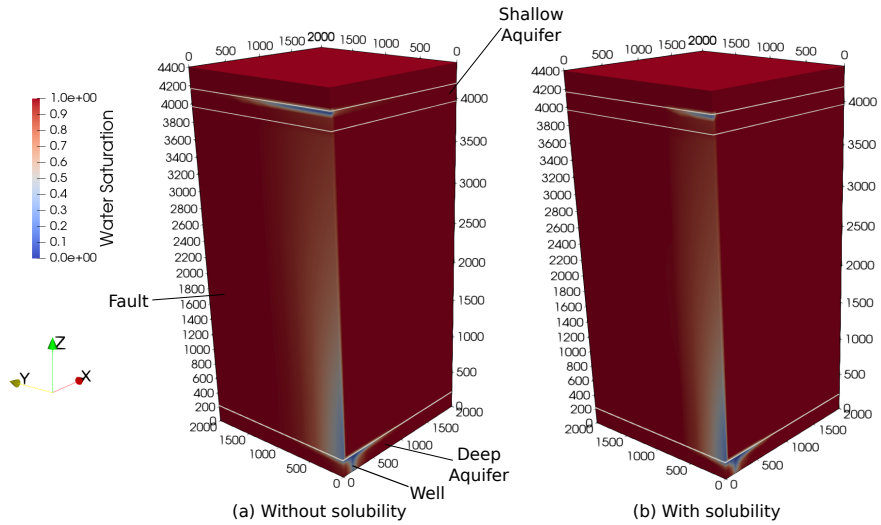


Figure 3: Corner cutout views of the water saturation field along the fault in the base case at the end of injection, where (a) does not include solubility effects and (b) includes solubility effects.

289 ear effects and interactions estimated from the completed runs can be taken
 290 as representative of the simulation physics. While linear relationships can be
 291 detected using Pearson coefficients, they do not necessarily show monotonic
 292 nonlinear effects. We use Spearman coefficients to estimate first-order nonlin-
 293 ear correlations between the input variables to ensure that significant nonlinear
 294 relationships do not exist between variables. Figures S.4 and S.5 show that the
 295 nonlinear monotonic relationships between variables is not significant, regard-
 296 less of CO_2 solubility. We therefore proceed with our analysis of the outputs
 297 and their first-order relationships to the inputs, noting that the inputs are un-
 298 correlated to a first-order and are generally uniformly distributed regardless of
 299 CO_2 solubility and thus can be used to draw conclusions about first-order effects
 300 on CO_2 and brine leakage rates and CFF.

301 3.3. Solubility effects on brine and CO_2 leakage rates

302 Brine and CO_2 leakage rates and their variations show that CO_2 dissolution
 303 does not significantly affect brine leakage rates but does strongly affect CO_2

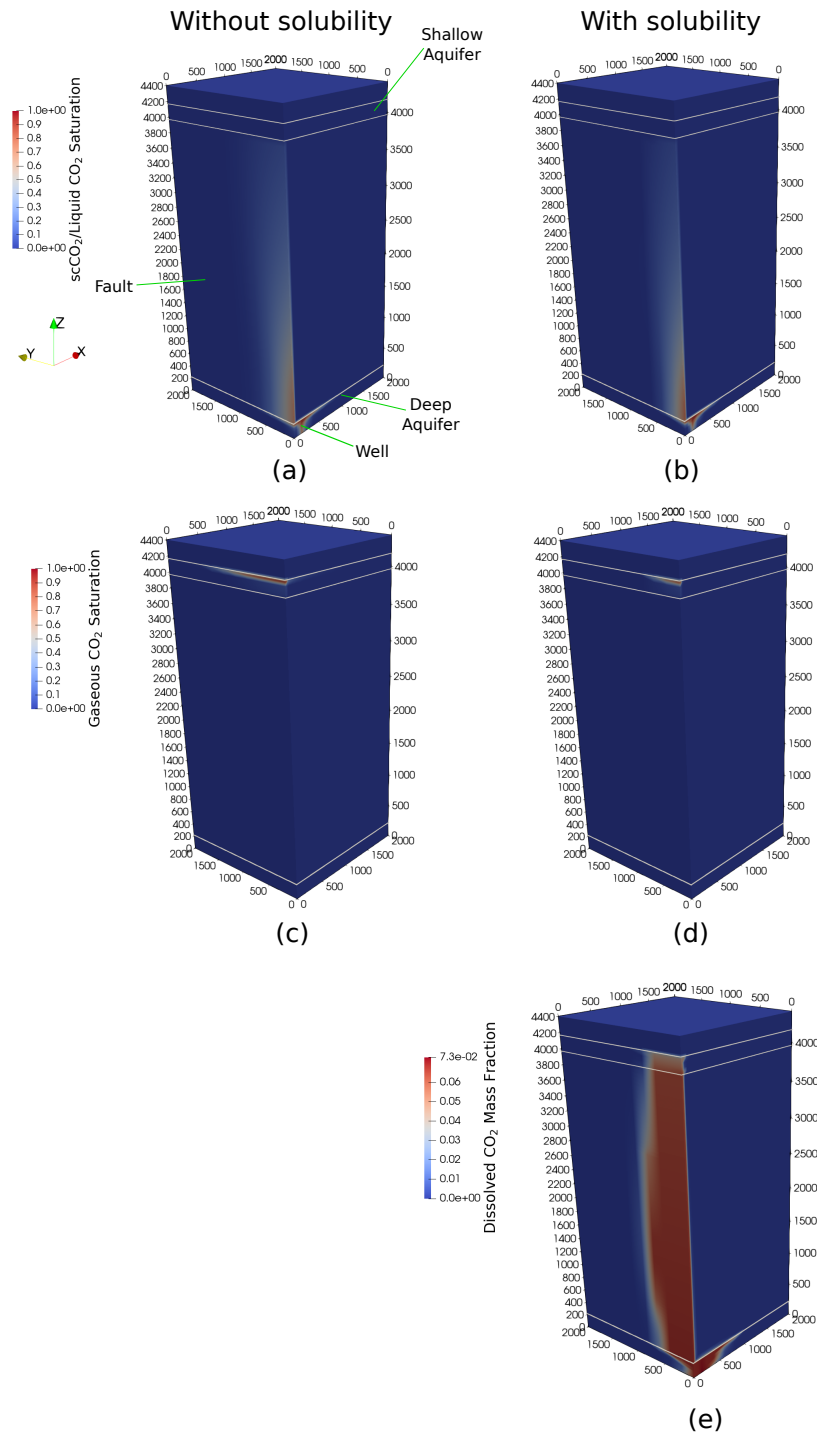


Figure 4: Corner cutout of CO₂ saturations along the fault in the base case at the end of injection, where (a) shows the scCO₂ saturation without solubility effects, (b) shows the scCO₂ saturation with solubility effects included, (c) shows the gaseous CO₂ saturation without solubility effects, (d) shows the gaseous CO₂ saturation with solubility effects included, and (e) shows the dissolved CO₂ mass fraction with solubility effects included.

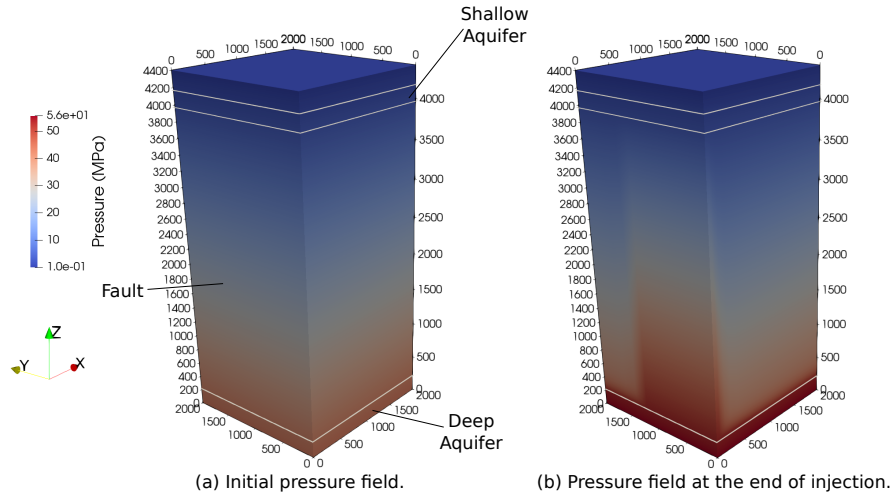


Figure 5: Corner cutout of pressure evolution in the fault in the base case, where (a) is the initial pressure field and (b) is the pressure field at the end of injection. The permeable length of the fault is evident in (b).

304 leakage rates, suggesting that solubility trapping, while potentially taking hun-
 305 dreds of years to reach its full potential (IPCC, 2005, Fig. 5.9), can change
 306 the rate of horizontal movement of free-phase CO_2 substantially in the first
 307 few years and decades of a CO_2 injection operation. As Figure 9 shows, the
 308 maximum brine leakage rates are largely clustered at low leakage rates for the
 309 range of parameters used in our study, with a moderate number reaching high
 310 leakage rates. The shape of the distribution is the same regardless of whether or
 311 not solubility effects are included. The distribution of maximum CO_2 leakage
 312 rates is starkly different with and without CO_2 solubility effects: when solubil-
 313 ity effects are included, a substantial proportion of simulations yield no CO_2
 314 leakage, as indicated by a jump in the cumulative distribution function (CDF)
 315 near zero. The CDF of CO_2 leakage rates reaches 1 at lower leakage rates when
 316 solubility is included. Using the maximum leakage rates as proxies for overall
 317 leakage, Figure 9 suggests that the inclusion of solubility effects increases the
 318 share of brine leakage relative to free-phase CO_2 leakage. This can be due to the
 319 free-phase CO_2 's horizontal mobility being reduced in the reservoir due to CO_2

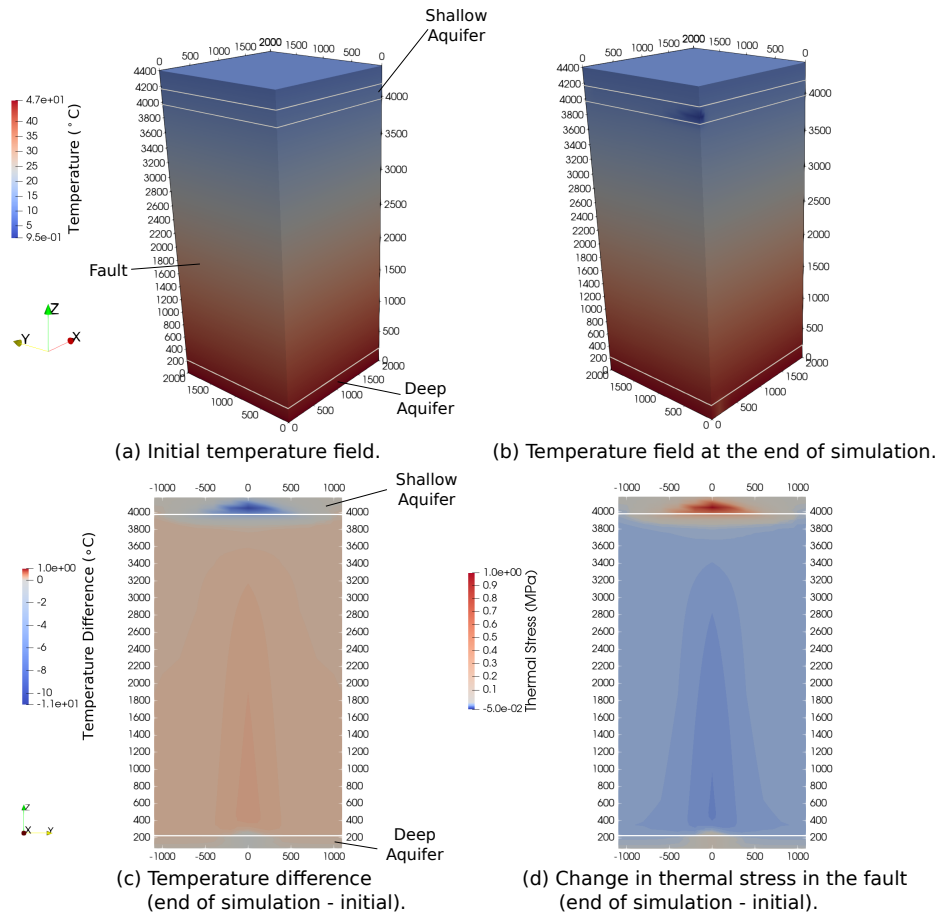


Figure 6: Corner cutout of temperature evolution in the fault in the base case, where (a) is the initial geothermal gradient, (b) is the temperature field at the end of the simulation, (c) is difference in temperature in the fault between the end of the simulation and the initial state, and (d) is the estimated thermal stress resulting from the temperature difference. Note that normal stress is positive in tension.



Figure 7: The CO₂ phase state as a function of depth in the fault under initial conditions.

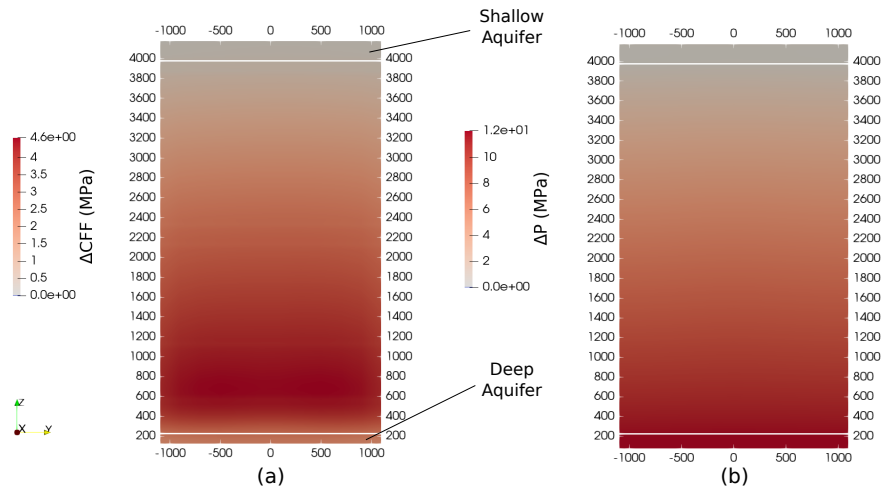


Figure 8: (a) ΔCFF and (b) pressure change from the initial pressure in the fault in the base case at the end of injection. Note that positive values of ΔCFF indicate fault destabilization.

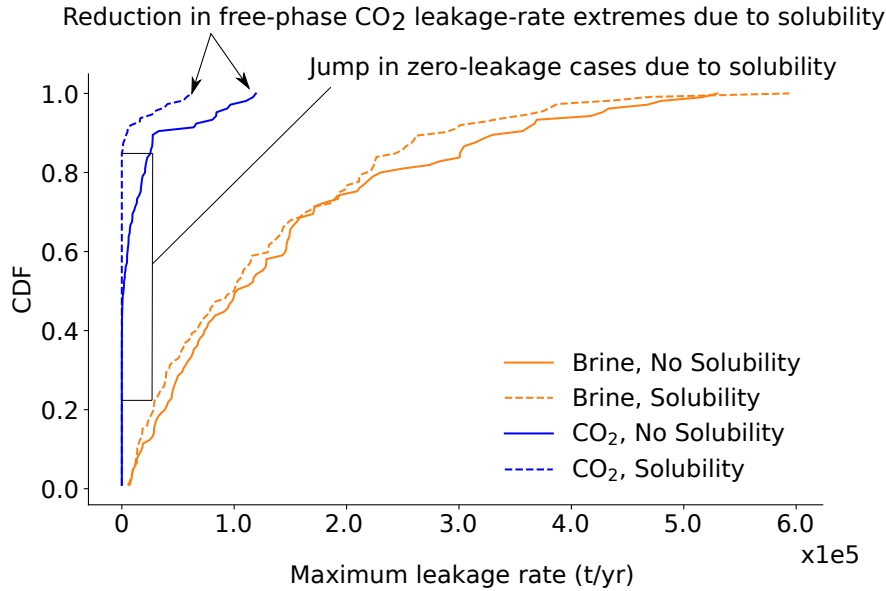


Figure 9: Cumulative distribution functions of the brine and CO₂ maximum end-year leakage rates (the maximum end-year leakage rate out of the 30 years of each simulation). The lower bound for denoting a zero-leakage case for CO₂ is 10^{-4} t/yr.

320 dissolution in the brine. After injection, the CO₂ rises toward the caprock and
 321 spreads thinly as a plume due to buoyancy. Since the edges of the plume consist
 322 of a thin layer of CO₂ in a large contact area with brine, dissolution may occur
 323 faster than during vertical migration of CO₂ toward the caprock. This dissolu-
 324 tion reduces the relative permeability of the edge of the CO₂ plume, resulting
 325 in substantially inhibited plume movement toward the fault. These results,
 326 along with results showing the impact of vertical grid resolution on CO₂ disso-
 327 lution (Pickup et al., 2010), suggest that solubility must be carefully considered
 328 when making fault-leakage ROMs with respect to free-phase CO₂ leakage rates.

329 3.4. Effects on fault reactivation

330 The poroelastic changes in the fault are sufficient to cause fault reactiva-
 331 tion, and the driving factor is the overpressure in the fault. Figures 10, 14,
 332 and 15 show results from the combined ensemble of 217 simulations, including
 333 those with and without solubility effects. Note that these figures show the en-

334 tire fault plane (the permeable fault location in Figure 2 and adjacent aquifer
 335 and caprock). Figure 10(a) shows that the overpressures in the lower portion
 336 of the fault (below $z = 1000$ m) can reach above 10 MPa relative to initial
 337 conditions. Figure 11 shows that the mode of the $\max(\Delta\text{CFF})$ across all runs is
 338 approximately 4 MPa. As $\Delta\text{CFF} = \Delta|\tau| + \mu_f \Delta\sigma'_n$ (Eqn. 1) and $\sigma'_n = \sigma_n + bp$,
 339 ΔCFF varies as $\mu_f bp$, where p is the pore pressure and σ_n is the total normal
 340 stress. In this case, $\mu_f b = 0.6 \times 0.8 = 0.48$, such that a 10 MPa overpressure
 341 causes a ΔCFF change of 4.8 MPa, which is close to the average of the values in
 342 Figure 11, with the difference being due to changes induced in the total traction
 343 and the shear traction. The overpressure values in Figure 10(a) in the lower
 344 portion of the fault also correspond to the maximum ΔCFF locations in Fig-
 345 ure 12. Note that Figure 11 shows that the presence of CO_2 solubility does not
 346 exert a clear impact on the distribution of $\max(\Delta\text{CFF})$, and Figure 12 shows
 347 that solubility does not affect the areal distribution of $\max(\Delta\text{CFF})$ in the fault.
 348 Figure 13 shows that virtually the entire fault permeable region experiences
 349 some degree of destabilization, which Figure 10(a) strongly suggests is due to
 350 pressurization. Pore pressure, regardless of CO_2 solubility, is the driving factor
 351 behind the fault destabilization.

352 The greatest uncertainties in overpressure are deep within the fault and
 353 within the uncertainty in the spatial extent of the permeable fault region. The
 354 standard deviation of overpressure (Figure 10(b)) shows that the greatest uncer-
 355 tainties in overpressure are at around $z = 425\text{-}675$ m and $y = \pm 700\text{-}900$ m, which
 356 reflect variability in the fault permeable length. These standard deviations reach
 357 about 6 MPa across the ensemble of runs (both soluble and insoluble). The stan-
 358 dard deviations are also larger immediately above the aquifer (which terminates
 359 at a depth of 225 m). Both the average overpressures and standard deviations of
 360 overpressure are substantially less significant at the top of the fault. The over-
 361 pressures in the fault tend to be higher the closer the y-coordinate is to those
 362 of the wells (0 m, ± 200 m), although the standard deviations of overpressure
 363 do not change significantly in the y-direction except at fault permeable region
 364 values. This shows that uncertainty in the fault permeable length introduces

365 significant uncertainty in the spatial distributions of overpressures, especially
366 deep within the fault.

367 The thermal stresses caused by temperature changes in the fault exhibit
368 significant destabilizing tensile stresses at the top of the fault, distinctly different
369 from the pressure distribution. Figure 10(a) shows the largest overpressures
370 below 1000 m depth, and Figure 10(b) shows the largest uncertainties also
371 below this depth. In contrast, the average temperatures in Figure 14(a) and
372 (c) show that there is mild heating in the fault but substantial cooling at the
373 top of the fault, with the amount of cooling increasing between the time of the
374 maximum ΔCFF (Figure 14(a)) and the end of the simulation (Figure 14(c)).
375 The standard deviations of these temperature changes are largest at the top of
376 the fault and increase with time (Figure 14(b) and (d)). This corresponds to the
377 phase transition from liquid CO_2 to gaseous CO_2 , during which the latent heat of
378 vaporization is absorbed from the environment and Joule-Thomson expansion
379 occurs, causing cooling (cf. Figure 7). The thermal stresses corresponding
380 to these temperature changes are mildly compressive in the fault and tensile
381 (destabilizing) at the top (Figure 15(a) and (c)). The standard deviations of
382 these thermal stresses are largest at the top and increase with time (Figure 15(b)
383 and (d)). The thermal stresses can potentially reactivate the fault at a shallow
384 depth, under the overburden, which is different from pressure-induced stresses,
385 which may result in fault reactivation slightly above the deep aquifer. Thermal
386 stresses seem benign or small outside of the region where CO_2 phase change
387 occurs. These observations are confirmed by a comparison of the magnitudes
388 of the thermal stresses versus the pore pressure increase in the fault, shown
389 in Figure 16. At the top of the fault (shown in Figure 16(a)), the thermal
390 stresses and fault's pore pressure increase are comparable in magnitude, albeit
391 different in timing (year of $\max(\Delta CFF)$ versus the end of the simulation). At
392 the bottom of the fault (shown in Figure 16(b)), the distributions of thermal
393 stresses and overpressures do not overlap, and the thermal stresses are negligible
394 compared to the overpressures. These results suggest that fault-leakage ROMs
395 should capture the phase-change path in the fault, possibly as a variable, to

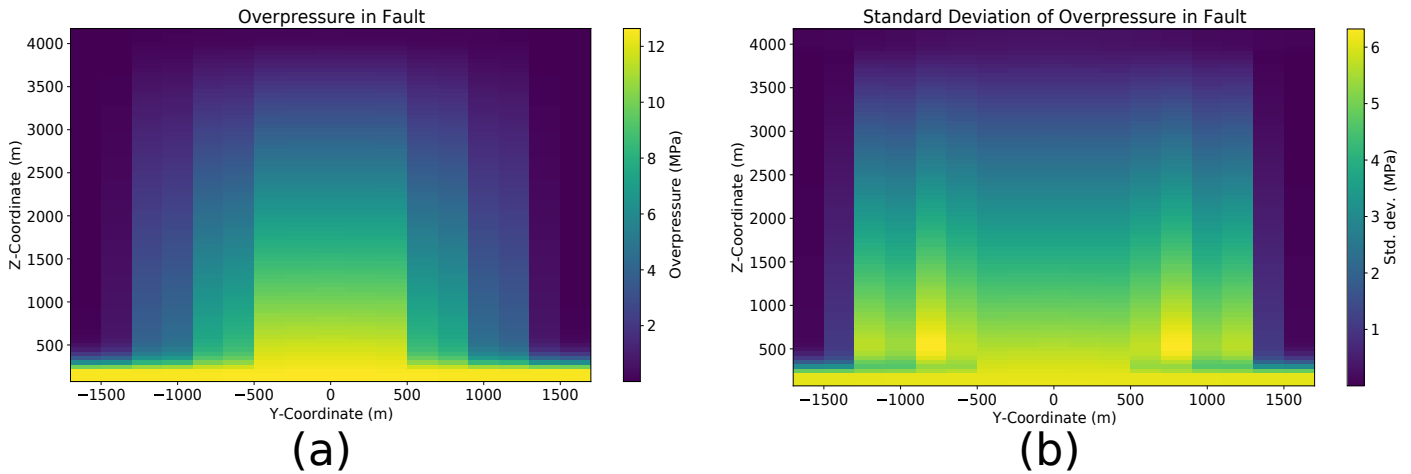


Figure 10: All changes shown are deviations from initial conditions. (a) Ensemble average of the *maximum* pressure adjacent to the fault. Pressures taken at the time of the $\max(\Delta\text{CFF})$ for each run in the ensemble. (b) Standard deviation of the ensemble pressures corresponding to (a).

396 incorporate the effects of thermal stresses on fault reactivation and possible
 397 leakage pathway creation. The CO_2 phase-change path is the sequential order
 398 of CO_2 phase states as CO_2 leaks up the fault based on the initial conditions.
 399 For example, Figure 7 shows that the CO_2 phase-change path in the base case
 400 is: sc CO_2 , liquid CO_2 , gaseous CO_2 . This path can, for example, be represented
 401 in a ROM by an indicator variable e.g. the path of sc CO_2 , liquid CO_2 , and then
 402 gaseous CO_2 can be represented by a 1 if it is reflective of the phase transitions
 403 in the fault of a given realization or 0 if it is not.

404 4. Discussion

405 4.1. Solubility in the Fault-Leakage Context

406 Solubility in GCS has been frequently studied within the context of a CO_2
 407 storage reservoir, but this study's novelty includes examining the effects of sol-
 408 ubility in the context of fault leakage. Extensive work has been done on solutal
 409 convection and density-driven fingering (Amooie et al., 2018; Ershadnia et al.,
 410 2020; Singh et al., 2021). The model problem studied in these papers has a

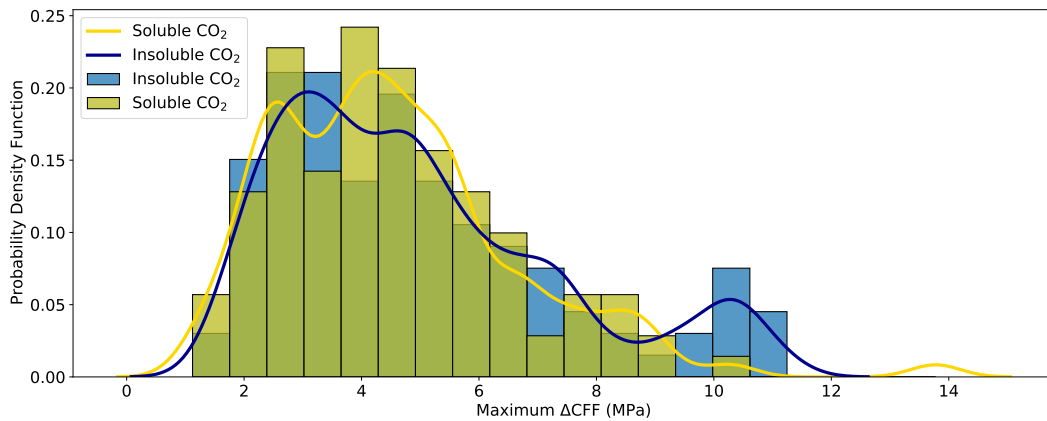


Figure 11: A histogram and kernel-density plot of the maximum ΔCFF values encountered in each run, both for runs with CO_2 solubility and those without CO_2 solubility. Note that the soluble CO_2 histogram overlays the insoluble CO_2 histogram and a third color appears where the two overlap.

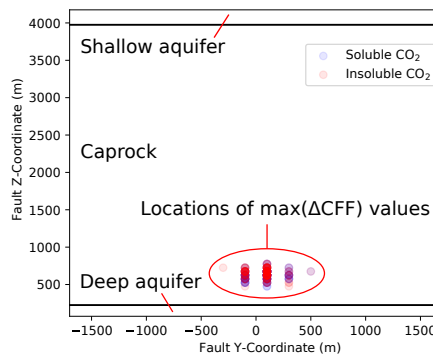


Figure 12: The locations of the points in the fault with the maximum ΔCFF change for each run. Note that while the runs including solubility and not including solubility were plotted separately, the points overlap.

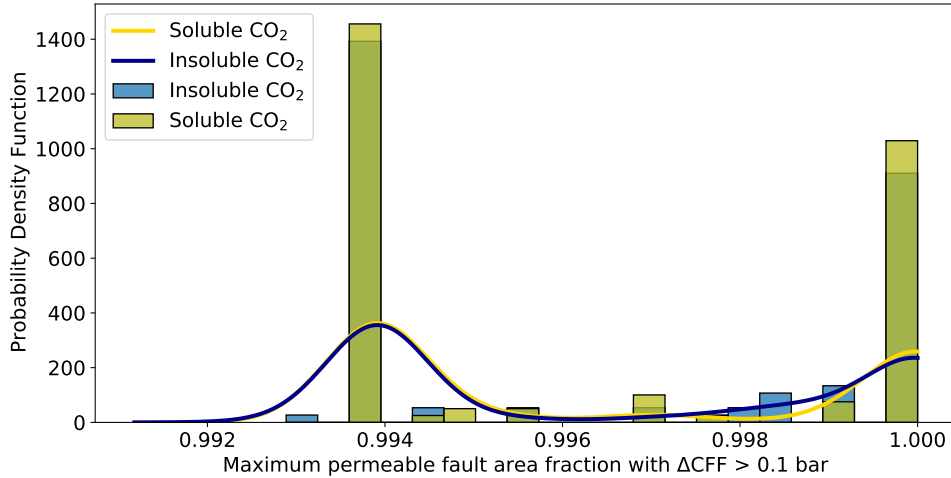


Figure 13: The fraction of the permeable area in the fault with $\Delta CFF > 0.1$ bar.

411 CO₂ plume positioned vertically above a brine column and migrating laterally
 412 beneath the bottom boundary of a caprock layer while gradually dissolving in
 413 brine. CO₂ dissolution causes density instabilities to form, causing fingering and
 414 convection due to the sinking of denser, CO₂-laden brine into the relatively less
 415 dense brine below. The consequence of such convection is increased solubility
 416 trapping in the storage reservoir. In contrast, solubility during fault-leakage
 417 is primarily a matter of CO₂ leakage-rate effects: as the fault itself would not
 418 be expected to store much CO₂, the effect of solubility manifests in the mag-
 419 nitude of free-phase CO₂ leakage. Figure 9 shows that brine leakage rates do
 420 not change much with solubility, although they do exhibit a slight shift toward
 421 lower leakage rates while free-phase CO₂ leakage rates decline substantially.
 422 Here, the flow in the fault is driven by the pressure gradient between the two
 423 aquifers and buoyant force due to the density difference between the CO₂ and
 424 brine phases. Nevertheless, CO₂ dissolution does occur within the fault and
 425 the storage reservoir. Unlike previous studies, which focused on the effects of
 426 solubility in the storage reservoir, this study shows an initial estimate of the
 427 effect of CO₂ solubility on the magnitude of free-phase CO₂ and brine leakage.

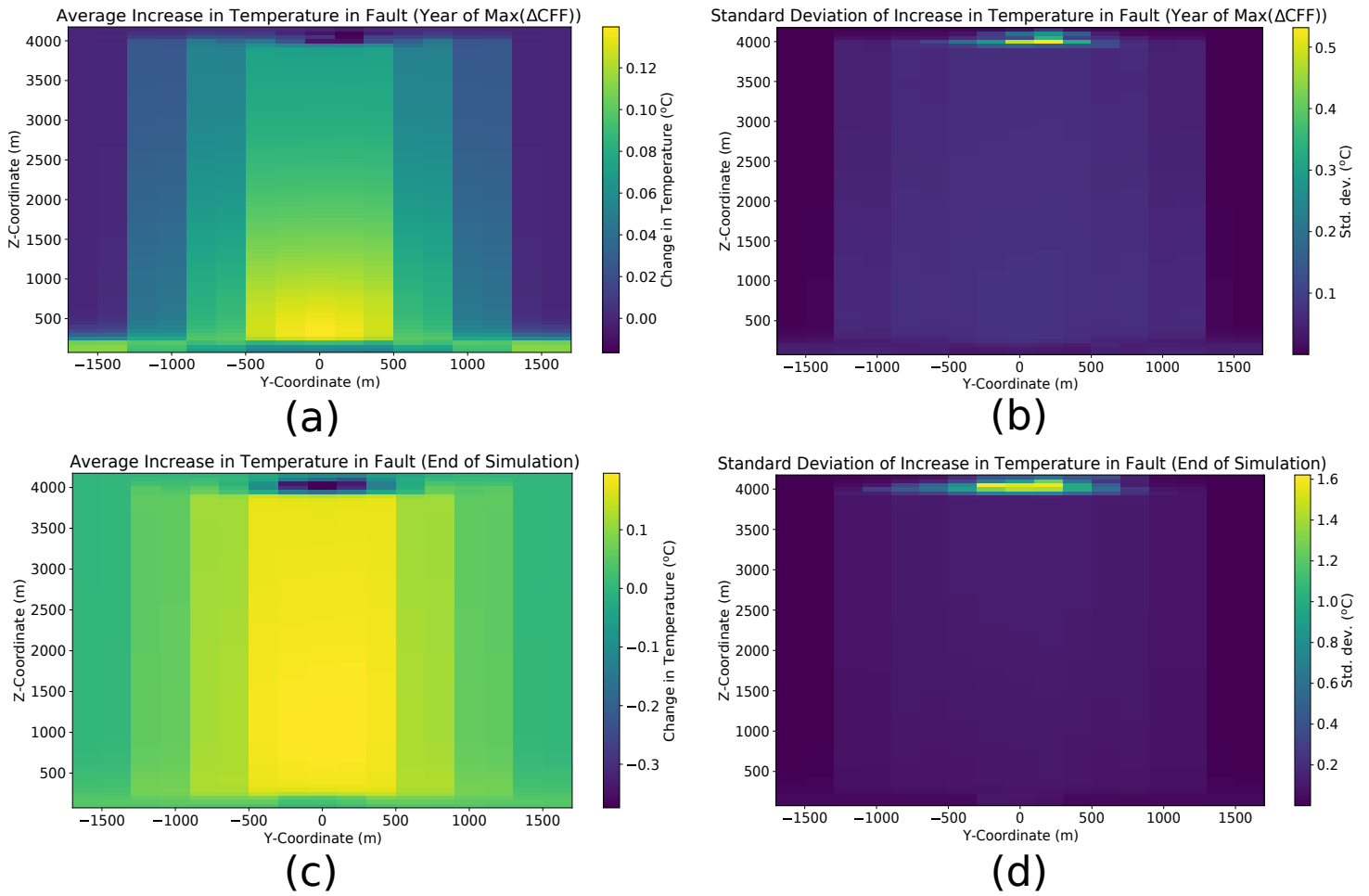


Figure 14: All changes shown are deviations from initial conditions. (a) Ensemble average of the *average* temperature adjacent to the fault. Temperatures taken at the time of the $\max(\Delta CFF)$. (b) Standard deviation corresponding to (a). (c) Ensemble average temperature increase in the fault at the end of the simulation. (d) Standard deviation of the ensemble temperatures in (c).

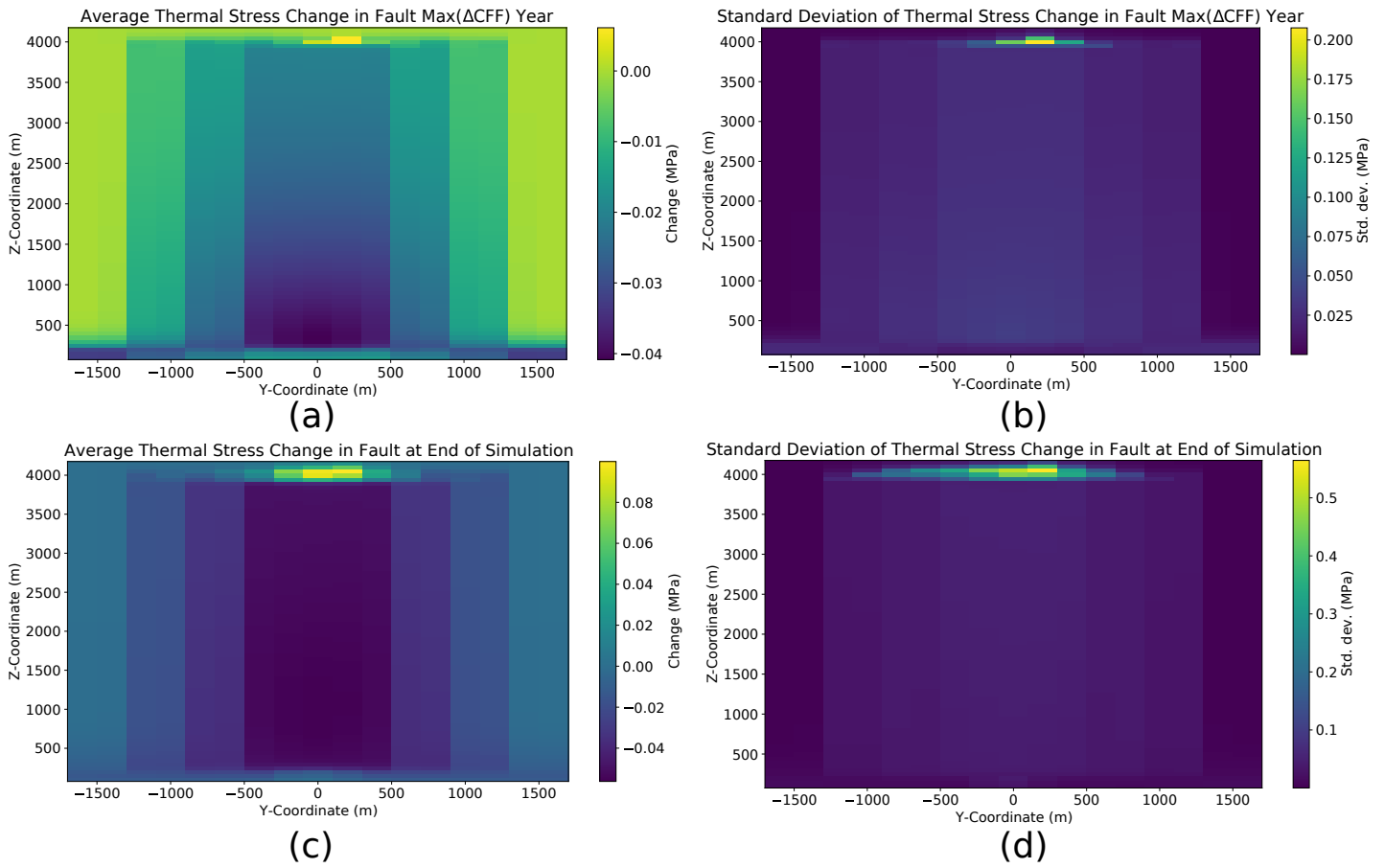
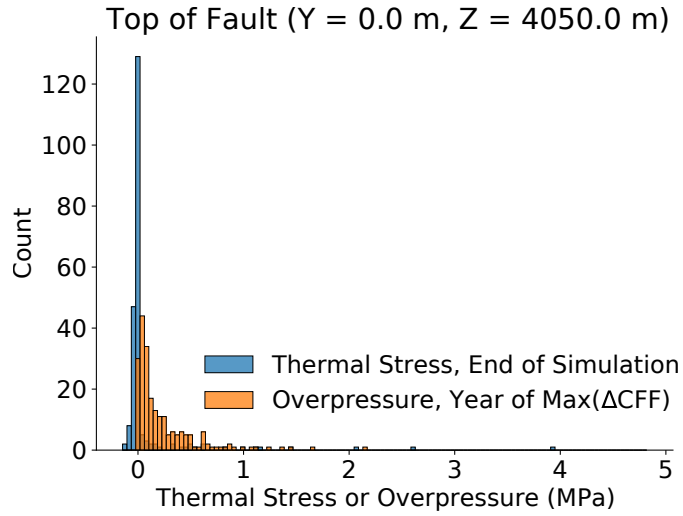
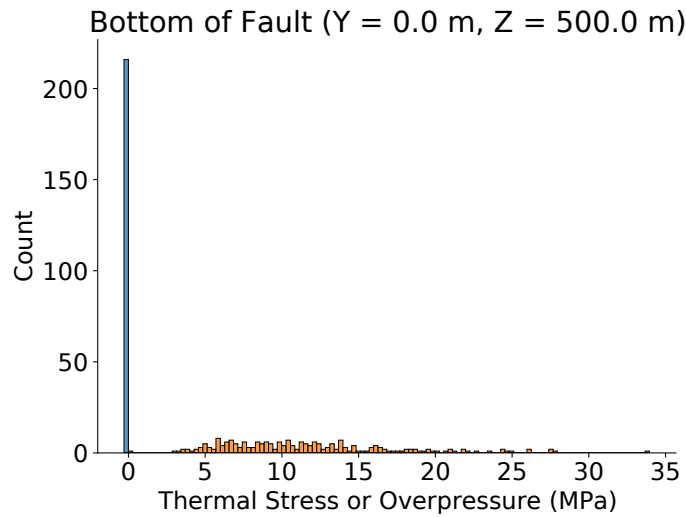


Figure 15: All changes shown are deviations from initial conditions. (a) Ensemble average thermal stresses corresponding to Fig. 14(a). (b) Standard deviation of the ensemble thermal stresses in (a). (c) Ensemble average thermal stresses corresponding to Fig. 14(c). (d) Standard deviation corresponding to (c).



(a)



(b)

Figure 16: Comparison of thermal stress and overpressure at the top and bottom of the fault. (a) The thermal stress (positive in tension) and the overpressure in the fault relative to the initial conditions at the top of the fault. (b) The thermal stress and the overpressure in the fault relative to the initial conditions at the bottom of the fault but slightly above the storage (deep) aquifer.

428 *4.2. Generalizability and Limitations for Real GCS Sites*

429 This study definitively shows that thermal stress changes can rival pore
430 pressure increases in faults during fault leakage if there are phase change-induced
431 temperature changes in the fault, a finding which impacts site evaluation for
432 operators. Recent studies have incorporated thermal effects in the case of fault
433 leakage behavior (Jung et al., 2015) and noted the importance of stress fields
434 in affecting failure, which then affects leakage pathways (Miocic et al., 2020).
435 This work connects these two lines of investigation by showing that thermal
436 stresses resulting from phase change-induced temperature changes during fault
437 leakage during GCS can affect stress fields enough (on the order of 1 MPa -
438 see Figure 16 and compare to a threshold of 0.1 bar (Reasenber & Simpson,
439 1992)) to induce fault failure and so potentially affect the leakage behavior. As
440 the changes in thermal stresses would tend to be concentrated near the phase-
441 change boundary from liquid to gaseous CO₂, operators should estimate the
442 phase-transition depth and use it to enhance their fault-seal analysis.

443 Given the simplified fault model, there are limitations to this study’s gener-
444 alizability, especially with respect to its modeling of a fault seal. Fault zones at
445 sites considered for GCS can be complex (Dockrill & Shipton, 2010; Mulrooney
446 et al., 2020), and the sealing capacity of a fault can vary widely depending on
447 factors such as the fault’s throw (Wu et al., 2021), fault-rock strength paramete-
448 rs (Rahman et al., 2021), and in-situ stresses (Rahman et al., 2021). Thermal
449 stresses induced by CO₂ phase change can also vary with the rock properties,
450 such as the thermal expansion coefficient or drained bulk modulus (Eqn. 2).
451 This study’s model also does not take into account differences in leakage due to
452 dip angle, which have been found to be important (Meguerdijian & Jha, 2021).
453 While CO₂ migration parallel to the fault is taken into account in this study, the
454 use of a fault seal analysis algorithm (e.g. the shale-gouge ratio (SGR) (Yielding
455 et al., 1997)) and the incorporation of dip angle would be helpful in a site study.

456 **5. Conclusions**

457 Thermal stresses and CO₂ solubility are phenomena that can affect the fault
458 stability and leakage rates during CO₂ leakage from a deep saline aquifer. In
459 this study, we find that:

- 460 1. Solubility effects can be neglected insofar as estimating poroelastic fault
461 reactivation or brine leakage rates are concerned, but solubility cannot be
462 neglected for estimating free-phase CO₂ leakage rates.
- 463 2. Thermal stresses can be more significant at shallow depths than at deep
464 depths in a fault when CO₂ phase change can take place, unlike pore
465 pressure changes, which are larger at deep depths in the fault.
- 466 3. Increases in tensile thermal stress post-injection can be sufficient to cause
467 failure in the fault when phase change is present.
- 468 4. Given the possibility of CO₂ phase change during fault leakage and the
469 associated thermal stresses, it may be advantageous to estimate the phase
470 change path of potentially leaking CO₂ and use it as a variable or param-
471 eter in fault-leakage ROMs.

472 We show that pore pressure and thermal stresses exhibit distinct effects in
473 different locations but that both can potentially cause fault reactivation. Future
474 work involves investigation of dip-angle effects on leakage rates and the creation
475 of fault-leakage ROMs.

476 **Declaration of Competing Interest**

477 The authors declare that they have no known competing financial interests or
478 personal relationships that could have appeared to influence the work reported
479 in this paper.

480 **Acknowledgements**

481 This work was supported by the U.S. Department of Energy through the
482 Los Alamos National Laboratory. Los Alamos National Laboratory is operated

483 by Triad National Security, LLC, for the National Nuclear Security Administra-
484 tion of the U.S. Department of Energy (Contract No. 89233218CNA000001).
485 This work was completed as part of the National Risk Assessment Partnership
486 (NRAP) project. Support for this project came from the U.S. Department of
487 Energy’s (DOE) Office of Fossil Energy’s Coal Research program.

488 The first author would like to acknowledge the support of the University of
489 Southern California’s Provost PhD fellowship.

490 References

491 (2019). 26 USC 45Q: Credit for carbon oxide sequestration. URL:
492 [https://uscode.house.gov/view.xhtml?req=\(title:26%20section:
493 45Q%20edition:prelim\).](https://uscode.house.gov/view.xhtml?req=(title:26%20section:45Q%20edition:prelim))

494 Amooie, M. A., Soltanian, M. R., & Moortgat, J. (2018). Solutal convec-
495 tion in porous media: Comparison between boundary conditions of con-
496 stant concentration and constant flux. *Physical Review E*, 98. URL:
497 <https://link.aps.org/doi/10.1103/PhysRevE.98.033118>. doi:10.1103/
498 PhysRevE.98.033118.

499 Bianchi, M., Zheng, L., & Birkholzer, J. T. (2016). Combining multiple lower-
500 fidelity models for emulating complex model responses for CCS environmen-
501 tal risk assessment. *International Journal of Greenhouse Gas Control*, 46,
502 248–258. URL: [https://www.sciencedirect.com/science/article/pii/
503 S1750583616300093](https://www.sciencedirect.com/science/article/pii/S1750583616300093). doi:10.1016/j.ijggc.2016.01.009.

504 Biot, M. A., & Willis, D. G. (1957). The Elastic Coefficients of the Theory
505 of Consolidation. *Journal of Applied Mechanics*, (pp. 594–601). URL: [http:
506 //www.pmi.ou.edu/Biot2005/papers/FILES/068.PDF](http://www.pmi.ou.edu/Biot2005/papers/FILES/068.PDF).

507 Burghardt, J., & Appriou, D. (2021). State of Stress Uncertainty Quan-
508 tification and Geomechanical Risk Analysis for Subsurface Engineering.
509 OnePetro. URL: [http://onepetro.org/ARMAUSRMS/proceedings/ARMA21/
510 A11-ARMA21/ARMA-2021-2129/468335](http://onepetro.org/ARMAUSRMS/proceedings/ARMA21/A11-ARMA21/ARMA-2021-2129/468335).

- 511 Caine, J. S., & Forster, C. B. (1999). Fault Zone Architecture and Fluid Flow:
512 Insights from Field Data and Numerical Modeling. In *Faults and Subsur-*
513 *face Fluid Flow in the Shallow Crust* (pp. 101–127). American Geophys-
514 ical Union (AGU). URL: [http://onlinelibrary.wiley.com/doi/abs/10.](http://onlinelibrary.wiley.com/doi/abs/10.1029/GM113p0101)
515 [1029/GM113p0101](http://onlinelibrary.wiley.com/doi/abs/10.1029/GM113p0101). doi:10.1029/GM113p0101.
- 516 Chester, F. M., Evans, J. P., & Biegel, R. L. (1993). Internal structure and
517 weakening mechanisms of the San Andreas Fault. *Journal of Geophysical*
518 *Research: Solid Earth*, *98*, 771–786. URL: [http://onlinelibrary.wiley.](http://onlinelibrary.wiley.com/doi/abs/10.1029/92JB01866)
519 [com/doi/abs/10.1029/92JB01866](http://onlinelibrary.wiley.com/doi/abs/10.1029/92JB01866). doi:10.1029/92JB01866.
- 520 Coussy, O. (2004). *Poromechanics*. West Sussex, England: John Wiley & Sons.
- 521 Dockrill, B., & Shipton, Z. K. (2010). Structural controls on leakage from a
522 natural CO₂ geologic storage site: Central Utah, U.S.A. *Journal of Structural*
523 *Geology*, *32*, 1768–1782. URL: [https://www.sciencedirect.com/science/](https://www.sciencedirect.com/science/article/pii/S0191814110000167)
524 [article/pii/S0191814110000167](https://www.sciencedirect.com/science/article/pii/S0191814110000167). doi:10.1016/j.jsg.2010.01.007.
- 525 Dor, O., Ben-Zion, Y., Rockwell, T. K., & Brune, J. (2006). Pulver-
526 ized rocks in the Mojave section of the San Andreas Fault Zone.
527 *Earth and Planetary Science Letters*, *245*, 642–654. URL: [https:](https://www.sciencedirect.com/science/article/pii/S0012821X06002548)
528 [//www.sciencedirect.com/science/article/pii/S0012821X06002548](https://www.sciencedirect.com/science/article/pii/S0012821X06002548).
529 doi:10.1016/j.epsl.2006.03.034.
- 530 Ershadnia, R., Wallace, C. D., & Soltanian, M. R. (2020). CO₂ geologi-
531 cal sequestration in heterogeneous binary media: Effects of geological and
532 operational conditions. *Advances in Geo-Energy Research*, *4*, 392–405.
533 URL: <https://www.yandy-ager.com/index.php/ager/article/view/277>.
534 doi:10.46690/ager.2020.04.05.
- 535 Guglielmi, Y., Birkholzer, J., Rutqvist, J., Jeanne, P., & Nussbaum, C. (2017).
536 Can Fault Leakage Occur Before or Without Reactivation? Results from
537 an in Situ Fault Reactivation Experiment at Mont Terri. *Energy Procedia*,
538 *114*, 3167–3174. URL: [https://linkinghub.elsevier.com/retrieve/pii/](https://linkinghub.elsevier.com/retrieve/pii/S1876610217316302)
539 [S1876610217316302](https://linkinghub.elsevier.com/retrieve/pii/S1876610217316302). doi:10.1016/j.egypro.2017.03.1445.

- 540 Harp, D. R., Pawar, R., Carey, J. W., & Gable, C. W. (2016). Reduced
541 order models of transient CO₂ and brine leakage along abandoned well-
542 bores from geologic carbon sequestration reservoirs. *International Jour-
543 nal of Greenhouse Gas Control*, 45, 150–162. URL: [https://linkinghub.
544 elsevier.com/retrieve/pii/S1750583615301493](https://linkinghub.elsevier.com/retrieve/pii/S1750583615301493). doi:10.1016/j.ijggc.
545 2015.12.001.
- 546 Helton, J. C., & Davis, F. J. (2002). *Latin Hypercube Sampling and the Prop-
547 agation of Uncertainty in Analyses of Complex Systems*. Sandia Report
548 SAND2001-0417 Sandia National Laboratories United States of America.
549 URL: <https://core.ac.uk/reader/194436110>.
- 550 IPCC (2005). *IPCC special report on carbon dioxide capture and storage*. Tech-
551 nical Report Intergovernmental Panel on Climate Change Cambridge Univer-
552 sity Press, UK.
- 553 Jacquey, A. B., Cacace, M., Blöcher, G., & Scheck-Wenderoth, M. (2015).
554 Numerical Investigation of Thermoelastic Effects on Fault Slip Tendency
555 during Injection and Production of Geothermal Fluids. *Energy Proce-
556 dia*, 76, 311–320. URL: [https://linkinghub.elsevier.com/retrieve/
557 pii/S1876610215016446](https://linkinghub.elsevier.com/retrieve/pii/S1876610215016446). doi:10.1016/j.egypro.2015.07.868.
- 558 Jha, B., & Juanes, R. (2014). Coupled multiphase flow and
559 poromechanics: A computational model of pore pressure effects on
560 fault slip and earthquake triggering. *Water Resources Research*,
561 50, 3776–3808. URL: [http://onlinelibrary.wiley.com/doi/10.1002/
562 2013WR015175/abstract](http://onlinelibrary.wiley.com/doi/10.1002/2013WR015175/abstract). doi:10.1002/2013WR015175.
- 563 Johri, M. (2012). *Fault Damage Zones - Observations, Dynamic Modeling, and
564 Implications of Fluid Flow*. Ph.D. thesis Stanford University Stanford, Cal-
565 ifornia. URL: [https://pangea.stanford.edu/departments/geophysics/
566 dropbox/SRB/public/docs/theses/SRB_131_OCT12_Johri.pdf](https://pangea.stanford.edu/departments/geophysics/dropbox/SRB/public/docs/theses/SRB_131_OCT12_Johri.pdf).
- 567 Jung, N.-H., Han, W. S., Han, K., & Park, E. (2015). Regional-scale
568 advective, diffusive, and eruptive dynamics of CO₂ and brine leakage

569 through faults and wellbores. *Journal of Geophysical Research: Solid*
570 *Earth*, 120, 3003–3025. URL: [http://onlinelibrary.wiley.com/doi/abs/](http://onlinelibrary.wiley.com/doi/abs/10.1002/2014JB011722)
571 [10.1002/2014JB011722](http://onlinelibrary.wiley.com/doi/abs/10.1002/2014JB011722). doi:10.1002/2014JB011722.

572 Keating, E. H., Fessenden, J., Kanjorski, N., Koning, D. J., & Pawar, R.
573 (2010). The impact of CO₂ on shallow groundwater chemistry: observations
574 at a natural analog site and implications for carbon sequestration. *Envi-*
575 *ronmental Earth Sciences*, 60, 521–536. URL: [https://doi.org/10.1007/](https://doi.org/10.1007/s12665-009-0192-4)
576 [s12665-009-0192-4](https://doi.org/10.1007/s12665-009-0192-4). doi:10.1007/s12665-009-0192-4.

577 Keating, E. H., Harp, D. H., Dai, Z., & Pawar, R. J. (2016). Reduced or-
578 der models for assessing CO₂ impacts in shallow unconfined aquifers. *In-*
579 *ternational Journal of Greenhouse Gas Control*, 46, 187–196. URL: [https:](https://linkinghub.elsevier.com/retrieve/pii/S1750583616300081)
580 [//linkinghub.elsevier.com/retrieve/pii/S1750583616300081](https://linkinghub.elsevier.com/retrieve/pii/S1750583616300081). doi:10.
581 [1016/j.ijggc.2016.01.008](https://linkinghub.elsevier.com/retrieve/pii/S1750583616300081).

582 Lindner, E. (2020). NRAP - Wednesday Morning Part 4 : NRAP fault
583 modeling: A new ROM for fault leakage. URL: [https://www.youtube.com/](https://www.youtube.com/watch?v=5QmfXMqDIUc&feature=youtu.be)
584 [watch?v=5QmfXMqDIUc&feature=youtu.be](https://www.youtube.com/watch?v=5QmfXMqDIUc&feature=youtu.be).

585 Lowell, R., Kolandaivelu, K., & Rona, P. (2014). Hydrothermal ac-
586 tivity. In *Reference Module in Earth Systems and Environmen-*
587 *tal Sciences*. Elsevier. URL: [https://www.sciencedirect.com/](https://www.sciencedirect.com/science/article/pii/B9780124095489091326)
588 [science/article/pii/B9780124095489091326](https://www.sciencedirect.com/science/article/pii/B9780124095489091326). doi:[https://doi.org/10.](https://doi.org/10.1016/B978-0-12-409548-9.09132-6)
589 [1016/B978-0-12-409548-9.09132-6](https://doi.org/10.1016/B978-0-12-409548-9.09132-6).

590 Lu, C., Sun, Y., Buscheck, T. A., Hao, Y., White, J. A., & Chiaramonte,
591 L. (2012). Uncertainty quantification of CO₂ leakage through a fault with
592 multiphase and nonisothermal effects. *Greenhouse Gases: Science and Tech-*
593 *nology*, 2, 445–459. URL: [http://onlinelibrary.wiley.com/doi/abs/10.](http://onlinelibrary.wiley.com/doi/abs/10.1002/ghg.1309)
594 [1002/ghg.1309](http://onlinelibrary.wiley.com/doi/abs/10.1002/ghg.1309). doi:<https://doi.org/10.1002/ghg.1309>.

595 Meguerdijian, S., & Jha, B. (2021). Quantification of fault leakage
596 dynamics based on leakage magnitude and dip angle. *International*

- 597 *Journal for Numerical and Analytical Methods in Geomechanics*, 45,
598 2303–2320. URL: <http://onlinelibrary.wiley.com/doi/abs/10.1002/nag.3267>. doi:10.1002/nag.3267.
- 600 Middleton, R. S., Chen, B., Harp, D. R., Kammer, R. M., Ogland-Hand,
601 J. D., Bielicki, J. M., Clarens, A. F., Currier, R. P., Ellett, K. M., Hoover,
602 B. A., McFarlane, D. N., Pawar, R. J., Stauffer, P. H., Viswanathan, H. S.,
603 & Yaw, S. P. (2020). Great SCO₂T! Rapid tool for carbon sequestration
604 science, engineering, and economics. *Applied Computing and Geosciences*,
605 7, 100035. URL: <http://www.sciencedirect.com/science/article/pii/S2590197420300173>. doi:10.1016/j.acags.2020.100035.
- 607 Miocic, J. M., Johnson, G., & Gilfillan, S. M. V. (2020). Stress field orienta-
608 tion controls on fault leakage at a natural CO₂ reservoir. *Solid Earth*, 11,
609 1361–1374. URL: <https://se.copernicus.org/articles/11/1361/2020/>.
610 doi:10.5194/se-11-1361-2020.
- 611 Mitchell, T. M., Ben-Zion, Y., & Shimamoto, T. (2011). Pulver-
612 ized fault rocks and damage asymmetry along the Arima-Takatsuki
613 Tectonic Line, Japan. *Earth and Planetary Science Letters*, 308,
614 284–297. URL: <https://www.sciencedirect.com/science/article/pii/S0012821X11002391>. doi:10.1016/j.epsl.2011.04.023.
- 616 Mulrooney, M. J., Osmond, J. L., Skurtveit, E., Faleide, J. I., &
617 Braathen, A. (2020). Structural analysis of the Smeaheia fault
618 block, a potential CO₂ storage site, northern Horda Platform, North
619 Sea. *Marine and Petroleum Geology*, 121, 104598. URL: <https://www.sciencedirect.com/science/article/pii/S0264817220303810>.
620 doi:10.1016/j.marpetgeo.2020.104598.
- 622 Newell, P., & Ilgen, A. G. (Eds.) (2019). *Science of Carbon Storage in Deep*
623 *Saline Formations*. Elsevier. URL: <https://linkinghub.elsevier.com/retrieve/pii/C20160032370>. doi:10.1016/C2016-0-03237-0.
- 624

625 Onishi, T., Nguyen, M. C., Carey, J. W., Will, B., Zaluski, W., Bowen,
626 D. W., Devault, B. C., Duguid, A., Zhou, Q., Fairweather, S. H., Span-
627 gler, L. H., & Stauffer, P. H. (2019). Potential CO₂ and brine leak-
628 age through wellbore pathways for geologic CO₂ sequestration using the
629 National Risk Assessment Partnership tools: Application to the Big Sky
630 Regional Partnership. *International Journal of Greenhouse Gas Control*,
631 *81*, 44–65. URL: [http://www.sciencedirect.com/science/article/pii/](http://www.sciencedirect.com/science/article/pii/S1750583618302329)
632 [S1750583618302329](http://www.sciencedirect.com/science/article/pii/S1750583618302329). doi:10.1016/j.ijggc.2018.12.002.

633 Pawar, R. J., Bromhal, G. S., Chu, S., Dilmore, R. M., Oldenburg, C. M.,
634 Stauffer, P. H., Zhang, Y., & Guthrie, G. D. (2016). The National Risk
635 Assessment Partnership’s integrated assessment model for carbon storage:
636 A tool to support decision making amidst uncertainty. *International Jour-
637 nal of Greenhouse Gas Control*, *52*, 175–189. URL: [https://linkinghub.](https://linkinghub.elsevier.com/retrieve/pii/S175058361630305X)
638 [elsevier.com/retrieve/pii/S175058361630305X](https://linkinghub.elsevier.com/retrieve/pii/S175058361630305X). doi:10.1016/j.ijggc.
639 2016.06.015.

640 Pickup, G., Kiatsakulphan, M., & Mills, J. (2010). Analysis of grid
641 resolution for simulations of CO₂ storage in deep saline aquifers.
642 European Association of Geoscientists & Engineers. URL: [https:](https://www.earthdoc.org/content/papers/10.3997/2214-4609.20144939)
643 [//www.earthdoc.org/content/papers/10.3997/2214-4609.20144939](https://www.earthdoc.org/content/papers/10.3997/2214-4609.20144939).
644 doi:<https://doi.org/10.3997/2214-4609.20144939>.

645 Rahman, M. J., Choi, J. C., Fawad, M., & Mondol, N. H. (2021). Proba-
646 bilistic analysis of Vette fault stability in potential CO₂ storage site Smea-
647 heia, offshore Norway. *International Journal of Greenhouse Gas Control*,
648 *108*, 103315. URL: [https://www.sciencedirect.com/science/article/](https://www.sciencedirect.com/science/article/pii/S1750583621000670)
649 [pii/S1750583621000670](https://www.sciencedirect.com/science/article/pii/S1750583621000670). doi:10.1016/j.ijggc.2021.103315.

650 Reasenber, P. A., & Simpson, R. W. (1992). Response of Regional Seismicity
651 to the Static Stress Change Produced by the Loma Prieta Earthquake. *Sci-
652 ence*, *255*, 1687–1690. URL: [https://science.sciencemag.org/content/](https://science.sciencemag.org/content/255/5052/1687)
653 [255/5052/1687](https://science.sciencemag.org/content/255/5052/1687). doi:10.1126/science.255.5052.1687.

- 654 Rinaldi, A. P., Rutqvist, J., & Cappa, F. (2014). Geomechanical ef-
655 fects on CO₂ leakage through fault zones during large-scale under-
656 ground injection. *International Journal of Greenhouse Gas Control*,
657 *20*, 117–131. URL: [http://www.sciencedirect.com/science/article/
658 pii/S1750583613003848](http://www.sciencedirect.com/science/article/pii/S1750583613003848). doi:10.1016/j.ijggc.2013.11.001.
- 659 Robertson, E. (1988). *Thermal properties of rocks*. USGS Numbered Series 88-
660 441 U.S. Geological Survey. URL: [http://pubs.er.usgs.gov/publication/
661 ofr88441](http://pubs.er.usgs.gov/publication/ofr88441).
- 662 Scholz, C. H. (2019). *The mechanics of earthquakes and faulting*. Cambridge
663 University Press. URL: <https://doi.org/10.1017/9781316681473>.
- 664 Sibson, R. H. (1977). Fault rocks and fault mechanisms. *Journal of the Ge-*
665 *ological Society*, *133*, 191–213. URL: [http://jgs.lyellcollection.org/
666 lookup/doi/10.1144/gsjgs.133.3.0191](http://jgs.lyellcollection.org/lookup/doi/10.1144/gsjgs.133.3.0191). doi:10.1144/gsjgs.133.3.0191.
- 667 Singh, M., Chaudhuri, A., Soltanian, M. R., & Stauffer, P. H. (2021). Coupled
668 multiphase flow and transport simulation to model CO₂ dissolution and local
669 capillary trapping in permeability and capillary heterogeneous reservoir. *In-*
670 *ternational Journal of Greenhouse Gas Control*, *108*, 103329. URL: [https:
671 //linkinghub.elsevier.com/retrieve/pii/S1750583621000815](https://linkinghub.elsevier.com/retrieve/pii/S1750583621000815). doi:10.
672 1016/j.ijggc.2021.103329.
- 673 Tiwari, D. K., Jha, B., Kundu, B., Gahalaut, V. K., & Vissa, N. K. (2021).
674 Groundwater extraction-induced seismicity around delhi region, india. *Scien-*
675 *tific Reports*, *11*.
- 676 Tran, M., & Jha, B. (2021). Effect of poroelastic coupling and fracture dynamics
677 on solute transport and geomechanical stability. *Water Resources Research*,
678 *57*, e2021WR029584. doi:<https://doi.org/10.1029/2021WR029584>.
- 679 White, J., Lu, C., & Chiaramonte, L. (2017). A Reduced-Order Model of
680 Fault Leakage for Second-Generation Toolset. URL: <https://www.osti.gov/>

681 servlets/purl/1433155/. doi:10.18141/1433155 Report Number: NRAP-
682 TRS-III-012-2017.

683 White, J. A., Castelletto, N., Klevtsov, S., Bui, Q. M., Osei-Kuffuor,
684 D., & Tchelepi, H. A. (2019). A two-stage preconditioner for mul-
685 tiphase poromechanics in reservoir simulation. *Computer Methods*
686 *in Applied Mechanics and Engineering*, 357, 112575. URL: [http:](http://www.sciencedirect.com/science/article/pii/S0045782519304402)
687 [//www.sciencedirect.com/science/article/pii/S0045782519304402](http://www.sciencedirect.com/science/article/pii/S0045782519304402).
688 doi:10.1016/j.cma.2019.112575.

689 White, J. A., & Foxall, W. (2016). Assessing induced seismic-
690 ity risk at CO₂ storage projects: Recent progress and remaining
691 challenges. *International Journal of Greenhouse Gas Control*, 49,
692 413–424. URL: [http://www.sciencedirect.com/science/article/pii/](http://www.sciencedirect.com/science/article/pii/S175058361630127X)
693 [S175058361630127X](http://www.sciencedirect.com/science/article/pii/S175058361630127X). doi:10.1016/j.ijggc.2016.03.021.

694 Wu, L., Thorsen, R., Ottesen, S., Meneguolo, R., Hartvedt, K., Ringrose, P., &
695 Nazarian, B. (2021). Significance of fault seal in assessing CO₂ storage capac-
696 ity and containment risks – an example from the Horda Platform, northern
697 North Sea. *Petroleum Geoscience*, 27. URL: [https://doi.org/10.1144/](https://doi.org/10.1144/petgeo2020-102)
698 [petgeo2020-102](https://doi.org/10.1144/petgeo2020-102). doi:10.1144/petgeo2020-102.

699 Yielding, G., Freeman, B., & Needham, D. T. (1997). Quantitative
700 Fault Seal Prediction. *AAPG Bulletin*, 81, 897–917. URL: [https://](https://doi.org/10.1306/522B498D-1727-11D7-8645000102C1865D)
701 doi.org/10.1306/522B498D-1727-11D7-8645000102C1865D. doi:10.1306/
702 522B498D-1727-11D7-8645000102C1865D.

703 Zhao, X., & Jha, B. (2019). Role of well operations and multiphase geome-
704 chanics in controlling fault stability during CO₂ storage and enhanced oil
705 recovery. *Journal of Geophysical Research: Solid Earth*, 124. doi:10.1029/
706 2019JB017298.

707 Zhao, X., & Jha, B. (2021). A new coupled multiphase flow–finite strain defor-
708 mation–fault slip framework for induced seismicity. *J. Comput. Phys.*, 433,
709 110178. doi:10.1016/j.jcp.2021.110178.

- 710 Zheng, F., Jahandideh, A., Jha, B., & Jafarpour, B. (2021). Geologic
711 CO₂ Storage Optimization under Geomechanical Risk Using Coupled-
712 Physics Models. *International Journal of Greenhouse Gas Control*, 110,
713 103385. URL: [https://www.sciencedirect.com/science/article/pii/](https://www.sciencedirect.com/science/article/pii/S1750583621001377)
714 [S1750583621001377](https://www.sciencedirect.com/science/article/pii/S1750583621001377). doi:10.1016/j.ijggc.2021.103385.
- 715 Zyvoloski, G. A., Robinson, B. A., Dash, Z. V., Kelkar, S., Viswanathan,
716 H. S., Pawar, R. J., Stauffer, P. H., Miller, T. A., & Chu, S. (2015). Soft-
717 ware Users Manual (UM) for the FEHM Application Version 3.1 - 3.X.
718 URL: https://www.lanl.gov/orgs/ees/fehm/docs/FEHM_UM_V3.3.0.pdf
719 [LA-UR-12-24493](https://www.lanl.gov/orgs/ees/fehm/docs/FEHM_UM_V3.3.0.pdf).
- 720 Zyvoloski, G. A., Robinson, B. A., Dash, Z. V., & Trease, L. L. (1999). Models
721 and Methods Summary for the FEHM Application. URL: [https://www.](https://www.lanl.gov/orgs/ees/fehm/pdfs/fehm_mms.pdf)
722 [lanl.gov/orgs/ees/fehm/pdfs/fehm_mms.pdf](https://www.lanl.gov/orgs/ees/fehm/pdfs/fehm_mms.pdf).